Analysis of Bistatic and Monostatic Sea Clutter

Riccardo Palamà, Maria S. Greco, Pietro Stinco, and Fulvio Gini

Dipartimento di Ingegneria dell'Informazione

University of Pisa, via G. Caruso 16, 56122 Pisa, Italy

ABSTRACT

In this work, we analyze the sea clutter data collected simultaneously by the bistatic and monostatic nodes of a S-band netted radar system. The analyzed radar system is the NetRad, developed by the University College London (UCL) and the datasets were collected with four different out-of-plane geometries. The aim of the analysis is to compare statistically the behavior of the bistatic and monostatic sea clutter for different geometries. In particular, we focus on the sea spikes, whose presence increases the probability of false alarm of the radar detector. The statistical analysis is carried out by comparing the empirical distribution of sea clutter data with some known heavy-tailed distributions and by studying the behavior of three statistical parameters, the kurtosis the Weibull and K+Noise shape parameter. An algorithm that separates the sea spikes from the Bragg background is implemented, in order to study in-depth the sea spikes statistics. To this aim, we examine the empirical distribution of the spike duration and of the interval between two subsequent spikes. The results of our analyses show that spikiness is higher for low values of the bistatic angle and that bistatic data are sometimes less spiky than monostatic ones only for horizontal polarization.

Keywords*: bistatic radar, bistatic clutter, clutter modeling, real clutter data, sea spikes.*

1 INTRODUCTION

One of the hardest problems to deal with for the development and the performance evaluation of a maritime radar system is the presence of clutter. For this reason, the research on signal processing techniques for new radars, such as bistatic, multistatic and MIMO radars, cannot leave aside a detailed analysis of bistatic clutter properties. In recent years, the development at University College London (UCL) of the NetRad system, a netted radar composed of a monostatic node and a widely separated bistatic node, and the following measurement campaigns have allowed the study of sea clutter in the case of out-of-plane bistatic geometry [1]-[5]. The aim of this work is to characterize the differences between monostatic and bistatic clutter data, which were collected simultaneously by varying the polarization and the bistatic geometry (different baselines and bistatic angles). The analyzed datasets were acquired in two different days during which the environmental conditions were quite similar in terms of wind velocity and sea state [6].

From a statistical point of view, sea clutter is typically considered as a stochastic process characterized by the presence of spikes, which are sequences of high-value samples, not expected in a Gaussian process, hence the terms *spikiness* and *spiky*, referred to clutter, are often used to indicate its deviation from Gaussianity. The analysis about the spikiness is usually made by examining the empirical probability density function (pdf), i.e. the histogram, of the clutter samples and by considering that the heavier its tail is the spikier the clutter is. In recent times, a growing attention has been devoted to the family of the Complex Elliptically Symmetric (CES) distributions, which includes the compound-Gaussian (such as K and *t*-Student) and Generalized Gaussian distributions and some recent works have shown their good fitting to measured radar clutter data [7].

Previous works [3] have dealt with the statistical analysis of sea clutter data which were simultaneously collected by the NetRad monostatic and bistatic nodes. In particular, Al-Ashwal *et al.* [5] analyze the behavior of the empirical cumulative distribution function (c.d.f) of the clutter amplitude and show that some data are best modeled by the KA distribution. The authors study also the spikiness of the data, by concluding that in many cases bistatic clutter is less spiky than monostatic one. Furthermore, the largest difference between bistatic and monostatic spikiness has been measured for horizontally polarized data and a bistatic angle close to 90°.

In the present paper, we compare the empirical pdf with some known distributions, such as the Weibull, *K*, *K* plus thermal noise, Log-Normal, *t*-Student, Generalized Gaussian [8], [9] and the study of clutter spikiness is deepened by analyzing the variation of the shape parameters of the Weibull and K-plus-noise distributions as a function of range.

The work published by Walker [10] provides a distinction among three different contributions to sea clutter, depending on the physical phenomenon that originates the radar returns: Bragg, whitecap and burst scattering. Other works distinguish only between the Bragg and non-Bragg scattering, that is generally indicated as sea spikes [11]. Furthermore, it has been demonstrated that sea spikes are strongly related to breaking waves and can be separated from the Bragg scattering, which is a background component ([12], [13]). In the literature, the identification of sea spikes has been performed by amplitude thresholding [12] or based on some sea spike parameters ([13]-[15]). The statistical analysis of sea spikes has been carried out also in [14]. Furthermore, a recent work [16] proposes an algorithm that separates the contribution of the persistent spikes, of long duration, and short discrete spikes by employing the Hough transform. The differences between the monostatic and bistatic sea clutter have their physical justification, since basically the amount of electromagnetic (e.m.) energy backscattered by one point of sea surface is not the same in all the scattering directions. In general, the bistatic radar cross section (RCS) of one clutter cell is strongly influenced by the bistatic geometry, the polarization and the roughness of the sea surface. Concerning the characterization of the clutter received by a bistatic radar system, some works (e.g. [17], [18]) have dealt with the simulation of the e.m. scattering from rough surfaces, including the sea. According to [18], the azimuth angles which minimize the bistatic backscattered returns are different in case of horizontal and vertical polarization. The work published by Arnold-Bos *et al.* [17] provides the theoretical background for the simulation of the bistatic radar returns depending on the environmental conditions and on the bistatic geometry. In [4] the authors analyze the average reflectivity of bistatic and monostatic sea clutter data for low and high sea states and the results show that the radar cross section of bistatic clutter is generally lower than the monostatic one, reaching a minimum around a bistatic angle of 90°. This behavior is common for low and high sea states, with a slightly larger difference for VV polarized data.

After this introduction, the rest of this paper is organized as follows. In Section 2, the characteristics of the system and of the analyzed datasets are illustrated. In Section 3, we report the time history plots and the Power-Range-Time (PRT) maps of the received clutter samples, in order to provide a general view of the sea clutter data. In Section 4, we examine the fitting between the empirical distribution of the clutter amplitude and some known heavy-tailed theoretical models. We also investigate the behavior of the kurtosis of the In-Phase (I) and Quadrature (Q) clutter components and of the shape parameters of the Weibull and K-plus-Noise distributions, that bring some information about the clutter spikiness.

The spectral analysis is illustrated in Section 5, which contains the Range-Doppler maps, obtained by estimating the clutter Power Spectral Density (PSD). In Section 6, we analyze sea spikes by

studying the distribution of the spike duration and the interval between two subsequent spikes. Finally, the summary of the results of our analysis and other remarks are reported in Section 7.

2 SYSTEM AND DATASET DESCRIPTION

The analyzed data were collected by the NetRad system during a measurement campaign realized in October 2010 at Scarborough, Cape Town, by researchers from University College London (UCL) and University of Cape Town (UCT). NetRad, which is an abbreviation of "netted radar", is a radar system working both in monostatic and in bistatic configuration, thus composed of two nodes that are synchronized in time by using two GPS Disciplined Oscillators (GPSDO) and a 5 GHz wireless link. The system has been designed to work also in multistatic configuration, employing more than two nodes and more than two GPSDOs. The synchronization channel does not interfere with the radar signal, whose carrier frequency is 2.4 GHz. The monostatic node consists of a transmitter and a co-located receiver, whereas each bistatic node operates only as a receiver. In the analyzed dataset, only one bistatic node was employed. The baseline that separates the two nodes was set at 1827m (L_1) and 728m (L_2) for the measurements made on 10 October and 21 October, respectively (see details in Tab.2). The radar transmits a train of chirp pulses and its main parameters are listed in Tab.1 [2,3].

The antennas work in vertical (VV) or horizontal (HH) polarization and were pointed with an elevation angle θ_{el} =-1° and a variable azimuth angle. The receive and transmit antennas were pointed to create a bistatic geometry consisting in an isosceles triangle, whose vertices are the two nodes and the intersection point between their antenna patterns. As an effect of this bistatic geometry, in the region illuminated by both the antennas the two-way bistatic range $r_b^{(2w)}$ is twice the one way monostatic range $r_m^{(1w)}$, then an equivalent one-way bistatic range $r_b^{(1w)}$, being equal to $r_b^{(2w)}/2$, can be used in the comparisons. In the following, we will indicate as $r = r_b^{(1w)} = r_m^{(1w)}$ the range for both the bistatic and monostatic nodes. The value of the bistatic angle is a function of the selected range *r* and the baseline *L,*

$$\beta(r, L) = 2\sin^{-1}\left(\frac{L}{2r}\right) \tag{1}$$

As shown in Fig.1, the illustrated geometry was obtained by pointing the bistatic antenna with an azimuth angle φ_1 and the monostatic node with an azimuth angle φ_2, supplementary to φ_1. Thus the boresights of the monostatic and bistatic antennas form the angle β =180° - 2φ_1 ,which is the bistatic

angle at the center of the beam intersection[1]. Hence the main contribution of the clutter power is concentrated in the area illuminated by both the antennas, which corresponds to a range interval $[r_1, r_2]$ given by

$$\begin{cases} r_1 = (L/2)\cos(\varphi_{HP}/2)/\cos(\varphi_1 - \varphi_{HP}/2) \\ r_2 = (L/2)\cos(\varphi_{HP}/2)/\cos(\varphi_1 + \varphi_{HP}/2) \end{cases} \quad (2)$$

where φ_{HP} indicates the half-power beamwidth along the azimuth direction.

The nodes are synchronized by a 5 GHz wireless link using two GPSDOs. Since these oscillators are independent, there is a difference between their oscillation frequencies, which causes a deviation of the relative phase between the signals from the bistatic and the monostatic nodes [3]. This relative phase appears to be time-varying and generally non-linear and makes the clutter spectrum to spread out and its side-lobes to raise. The phase correction was realized by subtracting the phase of the direct signal, i.e. the return from the range cell containing the transmitter, from the matched-filtered signal as in [3],[19]. Measurements were made by varying the azimuth angle and the polarization. In each file the number of received samples, for each acquisition, is $N_{rs} = N_p \times N_r$, where N_p=130000 is the number of pulse repetition intervals, corresponding to a total acquisition time of 130 seconds, and N_r=1024 is the number of samples per sweep, i.e. the number of range bins. The radar was located on a bay facing the Atlantic Ocean and the analyzed data were acquired on October 10 and October 21, 2010. The weather reports indicate that the wind speed was from 35 km/h to 55 km/h on October 10 and from 20 km/h to 30 km/h on October 21, and its direction was approximately 300° (North-West) on both the days [6]. From the information about the wind speed, the sea state was 4-5 (Beaufort scale) for all the datasets. Furthermore, as reported in [3], the wave direction was different between the two days, which could indicate different levels of development of the sea. Tab.2 summarizes the main properties of each analyzed dataset.

3 MEASURED CLUTTER DATA

3.1 *Time History of Amplitude Clutter Samples*

The time-history plots of the amplitudes clutter samples are shown in Fig.2 for a selected range cell of the bistatic and monostatic VV data. The data relate to the dataset 4 (φ_1 = 60°, φ_2 = 60°, L=1827 m) and the range cell under test (r_{CUT}) is 2000 m from the receivers, corresponding to a

[1] In this paper, β indicates the bistatic angle at the center of the beam intersection for each dataset, whereas $\beta(r)$ is the bistatic angle corresponding to the range r.

bistatic angle $\beta(r_{CUT,})$ = 54°. Although the monostatic data show a power level higher than the bistatic ones, the presence of spikes is evident in both cases. It could be noted that there is little correspondence between the spiking events of the two plots. For the bistatic data, one high spike with short duration is present at about 60 s, and then other long spikes occur at about 90 s and 115 s. On the other hand, the monostatic data show one high and short spike at 80 s and minor events at about 45 s and 55 s. Further time-history plots of amplitude clutter samples can be found in [5].

3.2 *Power-Range-Time (PRT) Maps*

The PRT maps have been obtained by considering the entire duration of the data. Fig.3 and Fig.4 show the PRT maps for β = 30°, (datasets 7-8) and β =60° (datasets 3-4), respectively. In the maps, the horizontal axis corresponds to the time in seconds, the vertical one to the range in meters and the color scale gives the power in dBmW. The considered range interval is where the bistatic clutter-to-noise power ratio (CNR) is high, that is approximately from 1000 m to 1350 m if β = 30° and from 1700 m to 2200 m if β = 60°. The limits of the considered range interval were observed both in the PRT maps and in the plots of CNR versus range in Fig.7, and show a good matching to the values of r_1 and r_2 calculated by (2). The range-time maps are characterized by bands of high power, i.e. the e.m. returns from the wave fronts. A great number of powerful scatterers can be located on the crest of the sea waves, and the velocity by which they migrate in range is related to the slope of the banded pattern in each map. By examining one range cell, this backscattering component lasts from one to about 3 seconds, thus it seems similar to the whitecap component of the Walker's model ([9],[10]). The third clutter component is given by the discrete sea spikes, which have a smaller duration – less than one second – and are supposed to be present only in HH polarization. Discrete and long-lasting spikes are generally considered as part of the same non-Bragg scattering component and can be noted mostly in the HH polarized data. On the other hand, the PRT maps shows a more uniform power level in the VV polarized data, which means that the Bragg scattering component influences strongly the sea clutter returns at vertical polarization. By examining Fig.3, for the dataset acquired on the 21st October 2010 the monostatic data show a banded pattern which is smoother than for bistatic data, which means that the shadowing effect on the scatterers not on the crest of the sea waves is stronger for the bistatic data. This can be caused by the geometry of the system, since those scatterers are located on the monostatic line of sight (l.o.s.) but not also on the bistatic one. Furthermore, by considering how the bistatic maps vary w.r.t. the bistatic angle - while keeping the baseline fixed - the banded pattern is more evident in the data with small bistatic angle (β = 30°), then its level decreases for β=50°. For both bistatic and

monostatic data the banded pattern vanishes almost totally in the datasets acquired on 10th Oct.2010, which may be due to different sea conditions. For the same datasets, the evidence of the banded pattern is minimum for $\beta = 60°$, and increases slightly for $\beta=90°$.

In conclusion the presence of the banded pattern is influenced mostly by the sea conditions. If the banded pattern is present, the bistatic geometry, and in particular the bistatic angle, has appeared as the most influential factor. The PRT maps suggest a strong relation between the presence of bands of high power and the occurrence of long-lasting spikes. This is justified by the fact that these long-lasting spikes occur on the crest of the sea waves - whose e.m. returns originate the banded pattern in the maps - probably when they are about to break. Nevertheless, the presence of discrete (short-lasting) spikes can be noted also where the e.m. return from the wave fronts is negligible (see Fig.4c). In general, discrete spikes occur mainly in horizontally polarized data, both for monostatic and bistatic, but in case of vertical polarization the bistatic data seem to have a higher number of discrete spikes than monostatic data. The behavior of the monostatic and bistatic data depending on the polarization is similar to that showed in [12] for monostatic clutter, since in general spikes occur mainly in horizontally polarized data.

4 STATISTICAL ANALYSIS

4.1 *I-Q Clutter Components*

We analyze here the behavior of the clutter complex envelope, $X=X_I+jX_Q$. The empirical pdf's of I and Q data are compared to a Gaussian (G) pdf and a Generalized Gaussian (GG) pdf, which is given by:

$$f_{X_I}(x) = f_{X_Q}(x) = \frac{\nu}{2\alpha\Gamma(1/\nu)}\exp\left(-\left|\frac{x}{\alpha}\right|^{\nu}\right) \tag{3}$$

where $\alpha > 0$ is the scale parameter, $\nu > 0$ is the shape parameter, and $\Gamma(.)$ denotes the Gamma function. The Gaussian distribution is a special case of the GG, for shape parameter $\nu = 2$ and scale parameter α equal to the standard deviation (std) of the data [7]. The I and Q components of the measured sea clutter data show a heavy-tailed behavior, which means that a considerable number of spikes occur in both HH and VV data. I-Q histograms fit closely the GG model, which provides good fitting also in the tail region. An example of the results is plotted in Fig.5, where we plot the histograms of the bistatic HH data for azimuth angle $\varphi_1= 65°$, for the range cell at 900 m.

For a deeper analysis of I and Q data non-Gaussianity, the kurtosis was also evaluated, since it measures the relative (w.r.t. the Gaussian one) peakedness or flatness of the data distribution. The kurtosis γ_4 of the random variable (r.v.) Y is defined by

$$\gamma_4 = \frac{E\left\{\left(Y-\mu_Y\right)^4\right\}}{E\left\{\left(Y-\mu_Y\right)^2\right\}^2} - 3 \ , \tag{4}$$

where $\mu_Y = E\{Y\}$. If Y is a Gaussian r.v. $\gamma_4 = 0$, whereas γ_4 assumes increasing values for heavier tailed distributions. In Tab.3 we show the values of kurtosis for the I and Q components, X_I and X_Q, averaged over an interval of ten range cells, centered on r_{CUT}. The center range cell was chosen among the cells with higher CNR, by examining the plots in Fig.7. By considering the center range cell r_{CUT} at 1400 m, the average kurtosis assumes the highest values for β=30° (acquired on 21/10/10). The difference is due to the different geometries, but, maybe as well, to different environmental conditions. The comparison between simultaneously collected bistatic and monostatic data shows that in the case of horizontal polarization, monostatic data assume generally higher values of kurtosis than bistatic ones, but the behavior is opposite for vertically polarized data.

4.2 *Clutter Amplitude*

The analysis of the data amplitude was performed by examining the fitting between the empirical pdf and the theoretical pdf's of some known distributions, which are the Weibull (W), *K*, Log-Normal (LN), and compound-Gaussian with Inverse Gamma texture (IG) or *t*-Student ([22], [23]). In addition to these models, which have been widely studied in literature, we also investigated the goodness of fitting of the K-plus-Noise (K+N) and of the Generalized Gaussian (|GG|) models. The empirical pdf of the data was estimated by computing the histograms over the N_P pulses collected from each selected range cell. The characteristic parameters of the theoretical pdf's were estimated by using the Method of Moments (MoM) [22]. Herein, we report the mathematical expressions of each utilized theoretical pdf $p_Z(z)$ and of its n-th order moment $E\{Z^n\}$, where $Z = |X|$ is the clutter amplitude in the cell under test.

a. Weibull (W)

$$p_Z(z) = \frac{c}{b}\left(\frac{z}{b}\right)^{c-1} \exp\left[-\left(\frac{z}{b}\right)^c\right] u(z) \tag{5}$$

$$E\{Z^n\} = b^n \Gamma(n/c+1) \tag{6}$$

where $b>0$ is the scale parameter and $c>0$ is the shape parameter, $\Gamma(.)$ is the Gamma function and $u(.)$ is the unit step function. The Rayleigh distribution is obtained by setting $c = 2$ (the smaller c the spikier the data).

b. K

$$p_Z(z) = \frac{\sqrt{2\nu/\mu}}{\Gamma(\nu)2^{\nu-1}} \left(z\sqrt{2\nu/\mu}\right)^{\nu} K_{\nu-1}\left(z\sqrt{2\nu/\mu}\right) u(z) \tag{7}$$

$$E\{Z^n\} = \frac{(2\mu/\nu)^{n/2}\,\Gamma(n/2+\nu)\Gamma(n/2+1)}{\Gamma(\nu)} \tag{8}$$

where $\mu>0$ is the scale parameter and $\nu>0$ is the shape parameter, $K_{\nu-1}(.)$ is the modified Bessel function of the third kind of order ν-1. The Rayleigh distribution is obtained for $\nu \to \infty$ (the smaller ν the spikier the data).

c. Log-Normal (LN)

$$p_Z(z) = \frac{\delta}{z\sqrt{2\pi}} \exp\left[-\frac{1}{2}\left(\vartheta + \delta \ln(z)\right)^2\right] u(z) \tag{9}$$

$$E\{Z^n\} = \exp\left[\frac{n}{\delta}\left(\frac{n}{2\delta} - \vartheta\right)\right] \tag{10}$$

where $\vartheta>0$ is the scale parameter and $\delta>0$ is the shape parameter. The Rayleigh distribution is obtained by setting $\delta = 0.5$ (the higher δ over 0.5 the spikier the data).

d. Compound Gaussian with Inverse Gamma texture (IG)

$$p_Z(z) = 2\eta z\left(1+\frac{\eta}{\lambda}z^2\right)^{-(\lambda+1)} u(z) \tag{11}$$

$$E\{Z^n\} = \frac{(\lambda/\eta)^{n/2}\,\Gamma(\lambda - n/2)\Gamma(n/2+1)}{\Gamma(\lambda)} \tag{12}$$

where $\eta>0$ is the scale parameter and $\lambda>0$ is the shape parameter. The Rayleigh distribution is obtained for $\lambda \to \infty$ (the smaller λ the spikier the data).

e. Generalized Gaussian Amplitude ($|GG|$)

$$p_Z(z) = \frac{\sigma z}{\alpha\Gamma(\sigma^{-1})s^{1/\sigma}} \exp\left[-\frac{1}{s}\left(\frac{z^2}{2\alpha}\right)^{\sigma}\right] u(z) \tag{13}$$

$$E\{Z^n\} = (2\alpha)^{n/2}\, s^{n/2\sigma}\Gamma\left(\frac{n+1}{2\sigma}\right)\Gamma^{-1}\left(\frac{1}{\sigma}\right) \tag{14}$$

where $s = \left[\Gamma\left(\sigma^{-1}\right)/\Gamma\left(2\sigma^{-1}\right)\right]^{\sigma}$, $\alpha>0$ is the scale parameter and $\sigma>0$ is the shape parameter. The Rayleigh distribution is obtained by setting $\sigma = 0.5$ (the smaller σ the spikier the data).

f. K plus thermal noise (K+N)

$$p_Z(z) = 2z\frac{b^{\nu}}{\Gamma(\nu)}u(z)\int_0^{\infty}\frac{x^{\nu-1}}{x+p_n}\exp\left\{\frac{-z^2}{x+p_n}\right\}\exp\{-bx\}dx \tag{15}$$

where b>0 is the scale parameter, ν>0 is the shape parameter and p_n is the thermal noise power. The Rayleigh distribution is obtained for $\nu \to \infty$ (the smaller ν the spikier the data). Since for this distribution, the even order moments have a closed form expression, the estimation of the three unknown parameters should involve the 6-th order moment, which is not robust since the variance of the estimators increases with the order of the moment. The problem can be simplified by extracting from the Range-Doppler map the noise level $\hat{p}_n$ on the frequency intervals where clutter is negligible (noise floor). Then the scale and shape parameters are estimated as shown in (16), by using the second and forth order moments, $\hat{m}_2 = \hat{E}\{r^2\}$ and $\hat{m}_4 = \hat{E}\{r^4\}$, estimated from the data as in [9].

$$\begin{aligned}\hat{b} &= \hat{\nu}/(\hat{m}_2 - \hat{p}_n)\\ \hat{\nu} &= 2(\hat{m}_2 - \hat{p}_n)^2/(\hat{m}_4 - 2\hat{m}_2^2)\end{aligned} \tag{16}$$

We focused on the range interval where bistatic-clutter power is high, since by moving away from this region, the contribution of the thermal noise is dominant. For the datasets acquired on 10th October 2010, the LN, K+N and IG models show to be a good fit for the data over the whole examined range interval, but only the LN pdf is able to follow the tails of the data histograms for those range cells where clutter power is very high. For the datasets collected on 21st October 2010, the data seem to be appropriately represented by the K model, but the good fitting of this model gets less precise in the cells where the CNR decreases. This is an expected result, since the K-distribution does not take into account the non-negligible effect of thermal noise [9]. The K-plus-Noise model is an extension of the K one and is obtained by adding a constant term (p_n), representing the thermal noise, to the Gamma-distributed texture (as shown in eq. (15)). The K+N distribution have a good fitting with the data over the entire analyzed range, also for low CNR

values (close to 5 dB). Weibull and |GG| distributions are not that far from the histograms but the fitting is good only on some range cells.

Some of these results on the amplitude fitting are shown in Fig.6, for bistatic HH and VV data, $\varphi_1 = 45°$ $r_{CUT} = 1380$ m (a and b), and $\varphi_1 = 60°$, $r_{CUT} = 1900$ m (c and d).

4.3 *Shape Parameter Analysis*

Some further information about the spikiness of the data is provided by the value of the shape parameter of one or more of the tested distributions. The shape parameter of a statistical distribution is often directly related to the shape of its tails, then it quantifies the deviation from Gaussianity of the data. It should be noted that in the analysis of the clutter amplitude the Gaussian nature is represented by a Rayleigh distributed r.v. For the Weibull distribution, decreasing values of the shape parameter c indicate an increasing deviation from Gaussianity. Typically, the values of c span the interval [0.5-2] and the lower c the spikier the clutter is. For the K+N distribution, decreasing values of its shape parameter ν_{K+N} [2] indicate an increasing deviation from Gaussianity, and for $\nu_{K+N} \rightarrow \infty$ it converges to a Rayleigh distribution. For each analyzed dataset, the values of c and ν_{K+N} were plotted as a function of the range. Fig.8 and Fig.9 show respectively the behavior of c and ν_{K+N} vs the range for all the analyzed datasets. The values of the CNR in the considered range cells can be read, for each dataset, in Fig.7. Figs.7 a, b, e and f show that for these datasets the average bistatic CNR is close to 10 dB, with peaks between 15 dB and 20 dB. On the other hand, Figs.7d, g and h show that, for some other datasets, the values of CNR is almost always higher than 15 dB., with wide range intervals where the CNR assumes values higher than 30 dB. The CNR is almost always higher in the monostatic data than in the bistatic ones.

As shown in Fig.8, the parameter c of bistatic HH data is generally higher than (or comparable with) that of the monostatic HH data. The behavior is different in VV polarized data, for which the bistatic parameter c is generally smaller than (or comparable with) the monostatic one.

The Weibull shape parameter assumes lower values for datasets 5-8 than for datasets 1-4, meaning that the former are spikier than the others. This is probably due to different sea conditions, different position of the analyzed clutter patch with respect to the shoreline, between the datasets acquired on 10th October 2010 (dataset 1-4) and those acquired on 21st October 2010 (5-8).

The behavior of K-plus-Noise shape parameter ν_{K+N} (see Fig. 9) as a function of range show a good agreement with that of the Weibull shape parameter. This is evident by comparing, for

[2] In this section, we denote by ν_{K+N} the shape parameter of the K-plus-Noise distribution, in order to distinguish it from the shape parameter ν of the "pure" K distribution.

instance, Fig.8h and Fig.9h. In some plots, the K+N shape show sharp variations, but its overall behavior is similar to the behavior of the Weibull shape parameter.

In addition, Tab.4 provides the values of ν_{K+N} for each analyzed dataset, averaged over an interval of ten range cells. This interval is centered on a range cell under test (r_{CUT}), selected within the high-CNR region (same interval used for average kurtosis values in Tab.3).The comparison between the values of simultaneous acquisitions seems to confirm that bistatic VV data are spikier than monostatic VV ones, while the spikiness of bistatic and monostatic HH data is comparable.

5 SPECTRAL ANALYSIS

5.1 *Range-Doppler Maps*

The Power Spectral Density (PSD) was estimated for each range cell in order to build the Range-Doppler maps for each analyzed dataset. The method adopted to estimate PSD was the Welch periodogram, with a window of 512 samples and an overlap of 50% [21]. Finally, Range-Doppler maps were plotted from the estimated PSDs. Fig.10a shows an example of the results, that is the map of the data collected by the bistatic node in case of horizontal polarization and bistatic angle β=50° (dataset 1). Fig.8b shows the Range-Doppler map of the simultaneously collected monostatic data. It is easy to note that the bistatic clutter is contained within a well-defined range interval, between 750 m and 1250 m, with the strongest peak in the range 850 m-1100 m. The bistatic clutter spectra are limited in range because of the geometry, whereas the monostatic ones show only an attenuation with increasing range. From the analysis of all the data, the clutter spectra show a higher power level, a higher center frequency and a larger bandwidth for the datasets collected on 21/10/10. What we show in Fig.10 is, of course, the average (in time) spectral behavior of the clutter, since each periodogram was calculated over a time interval of 130 seconds. The time-variability of the clutter spectrum and the effect of short scattering phenomena could be studied by plotting a Time-Doppler map of the data for a fixed range cell. An example of the analysis of the time-varying behavior of the bistatic sea clutter spectra can be found in [2], for the dataset collected on 10th October 2010.

The bistatic spectra are centered on a positive normalized Doppler frequency, which is justified by the fact that the angle formed by the sea waves direction - in most cases it is the same as the wind direction - and the bistatic bisector influences the value of the center frequency of the bistatic clutter spectrum. Once indicated as ψ the aspect angle of the sea waves direction with respect to the bistatic bisector in the illuminated clutter patch, the bistatic Doppler frequency f_b is

$$f_b = \left(\frac{2 f_c}{c_l} v \right) cos\psi \, cos\left(\frac{\beta}{2} \right) , \tag{17}$$

where v is the sea waves speed, f_c is the carrier frequency and c_l is the speed of light [20]. Fig.10 shows that the spectrum is centered on a value of normalized frequency close to 0.1, which yields a bistatic Doppler frequency equal to 100 Hz, by accounting that the PRF is 1 KHz. Once considered that the aspect angle ψ is close to 10°, the resulting sea waves speed is about 25 km/h, which is included into the range of values assumed by the wind speed at the time of the measurements, according to the forecast reports [6].

6 SEA SPIKES ANALYSIS

6.1 *Sea Spikes Classification*

Once analyzed the behavior of the measured data, we separated the spikes from the background. The classification of spikes was made by using the algorithm illustrated in [15]. Spikes are short echoes with an amplitude much higher than the background. Due to this observation, the implemented algorithm identifies a spike by using three parameters, which are the power threshold λ_p, the minimum spike width d_{min} and the minimum interval between spikes i_{min}. Those sets of samples which have a power level higher than λ_p and last longer than d_{min} are classified as spikes, and those spikes which are separated by an interval smaller than i_{min} are joined together to form one spike [15]. The power threshold was set as 6 times the mean power of the received returns, the minimum spike width was 80 ms and the minimum interval between spikes was 150 ms. These values were chosen empirically, by evaluating the performance of the spike selection algorithm in the time-history plots of clutter samples and in the masks of selected spikes. Fig.11a shows the time history of amplitude clutter samples (dataset 4), with the selected spikes highlighted in red. Fig.11b shows the mask of the selected sea spikes (bistatic data of dataset 4, same range interval of the PRT maps in Fig.4), where a white pixel corresponds to a spiky sample. The figures confirm a quite good classification of the spiking events.

6.2 *Statistical Analysis*

In this section we analyze the statistics of the spike width d and of the time interval between spikes i, by computing the histograms of the data and comparing them with the exponential pdf. This analysis was performed after that the sea spikes had been separated from the background. The theoretical pdf of the spike width, denoted as $p_D(d)$ in (18), is a one-sided exponential [15], shifted by d_{min}, with the same mean value of its empirical pdf, denoted as $\bar{d}$:

$$p_D(d) = \frac{1}{\bar{d}} exp\left(-\frac{d - d_{min}}{\bar{d}}\right) u(d - d_{min}) \tag{18}$$

Similarly, the theoretical pdf of the interval between spikes, $p_I(i)$, has the same mean value of the data, $\bar{i}$, and is shifted by i_{min} [15]:

$$p_I(i) = \frac{1}{\bar{i}} exp\left(-\frac{i - i_{min}}{\bar{i}}\right) u(i - i_{min}) \tag{19}$$

Fig.12 and Fig.13 show that the exponential distribution can model the distribution of the spike width and of the interval between spikes, but there are some deviations for values of i included between 10 s and 15 s. The deviations from the exponential model are present also in other analyzed data and they are sometimes evident as secondary peaks in the empirical distributions. A possible justification is the fact that the spikes classification algorithm does not distinguish the two different components, i.e. persistent and discrete spikes, which have different temporal characteristics and are caused by different physical phenomena. Some important information about the spikiness of each data can be extracted from Tabs. 5-6-7-8, which contain respectively the values of the mean spike width, the mean interval between spikes and the ratio between the number of samples belonging to a spike (N_{sp}) and the number of received samples (N_{rs}). In general, the number of spikes is the highest in the case of β=30°. The mean spike width is higher for β=30° (datasets 7-8) and β=50° (datasets 5-6) compared with β=60° (datasets 3-4) and β=90° (datasets 1-2). We also observe that bistatic data have longer spikes than monostatic data in case of vertical polarization, which is true also for most of the horizontal polarized data. The values assumed by the mean interval between spikes are generally higher for bistatic data than for monostatic.

7 CONCLUSIONS

This work addresses the analysis of sea clutter data collected simultaneously from the monostatic and bistatic nodes of the NetRad. The analysis of the measured clutter data has highlighted the presence of a banded pattern in the Power-Range-Time maps, which is generally more evident in bistatic data than in monostatic data. This banded pattern is due to the e.m. return from the wave fronts and its presence appears as related to the occurrence of powerful long-lasting spikes, similar to whitecaps. The presence of spiking events of short duration has been also observed within the banded pattern, where it is present, but discrete spikes occur also in datasets for which the banded

pattern vanishes. It has been shown that the banded pattern is more evident for the datasets collected on October 21, which is probably due to different sea conditions. The combined effect of discrete and long-lasting spikes is considered as non-Bragg scattering, which differs from the Bragg background component. In general, for the VV data the power level is more uniform, then the Bragg component is stronger than in HH data. The spikiness of each dataset has been statistically analyzed by evaluating the variation of the shape parameter of the Weibull and K-plus-Noise distributions as a function of range and the values of the kurtosis for a range cell selected within the region of high bistatic-clutter. The analysis also revealed that the data collected on 21st October 2010 have a higher spikiness, due to low values of the Weibull and K-plus-Noise shape parameters and higher values of kurtosis.

By considering the variation with respect to the polarization, bistatic VV data have shown to be often spikier than monostatic VV ones, which is not the case for HH polarization. However, for some of the analyzed data, the level of spikiness of bistatic and monostatic data is comparable, particularly for HH data. For the datasets collected on October 10, the LN and K+N models have shown to be a good fit for the distribution of the amplitude of clutter samples. On the other hand, Weibull and |GG| distributions have a good fit with the data for the datasets of October 21. It is worth remembering that the measurements were made with large baseline (1827 m) on the first day and with small baseline (728 m) on the second day, thus there are some differences on the positions of the nodes on the seacoast. Secondly, the wind speed was slightly smaller on October 10 than on October 21, even if the wind direction was almost the same.

The analysis of the distribution of the spike width and the interval between two subsequent spikes has revealed that both the parameters are fitted accurately by a shifted exponential distribution, particularly for the spike width. Moreover, he analysis of the statistical properties of sea spikes has shown that bistatic spikes last longer and are less frequent in time than monostatic ones.

In future work, we will analyze the variation of sea clutter spectra as a function of time, with the aim of examining the time-varying behavior of bistatic clutter spectra and of their statistics.

References

[1] Inggs, M., Balleri, A., Al-Ashwal, W. A., Ward, K. D., Woodbridge, K., Ritchie, M., Miceli, W., Tough, R. J A, Baker, C. J., Watts, S., Harmanny, R., Stove, A., Sandenbergh, J. S.,

Griffiths, H.D., "NetRAD multistatic sea clutter database", *Proceedings of the IEEE International Geoscience and Remote Sensing Symposium (IGARSS),* 2937-2940, Munich, Germany, Jul. 2012.

[2] Ritchie, M.A., Al-Ashwal, W.A., Stove, A.G., Woodbridge, K., and Griffiths, H.D., "Coherent analysis of horizontally-polarized monostatic and bistatic sea clutter", *Proceedings of the IET International Conference on Radar Systems (Radar 2012),* 1-5, Glasgow,UK, Oct. 2012.

[3] Al-Ashwal, W.A., *Measurement and Modelling of Bistatic Sea Clutter*, PhD thesis, University College London, 2011.

[4] Al-Ashwal, W.A., Woodbridge, K., Griffiths, H.D., "Analysis of bistatic sea clutter – Part I: Average reflectivity", *IEEE Transactions on Aerospace and Electronic Systems,* 50,2 (2014), 1283-1292.

[5] Al-Ashwal, W.A., Woodbridge, K., Griffiths, H.D., "Analysis of bistatic sea clutter – Part II: Amplitude statistics", *IEEE Transactions on Aerospace and Electronic Systems,* 50,2 (2014), 1293-1303.

[6] Weather Forecast and Reports, www.wunderground.com . Last access: October 6, 2014.

[7] Ollila, E., Tyler, D.E., Koivunen, V., and Poor, H.V. "Complex Elliptically Symmetric Distributions: Survey, New Results and Applications", *IEEE Transactions on Signal Processing*, 60, 11 (2012),5597-5625.

[8] Billingsley, J.B., Farina, A., Gini, F., Greco, M. and Verrazzani, L., "Statistical analyses of measured radar ground clutter data", *IEEE Transactions on Aerospace and Electronic Systems,* 35,2 (1999), 579 – 593.

[9] Ward, K.D., Tough, R.J.A, and Watts, S., *Sea Clutter: Scattering, the K Distribution and Radar Performance*, IET, London, UK, 2006.

[10] Walker, D., "Doppler modelling of radar sea clutter", *IEE Proceedings -Radar, Sonar and Navigation,* 148, 2 (Apr. 2001),73-80.

[11] Watts, S., "Modeling and simulation of coherent sea clutter", *IEEE Transactions on Aerospace and Electronic Systems,* 48, 4 (2012), 3303-3317.

[12] Melief, H.W, Greidanus, H., Van Genderen, P., and Hoogeboom, P. "Analysis of sea spikes in radar sea clutter data", *IEEE Transactions on Geoscience and Remote Sensing*, 44, 4 (2006), 985-993.

[13] Posner, F., and Gerlach, K., "Sea spike demographics at high range resolutions and very low grazing angles", *Proceedings of the IEEE Radar Conference,* 38-45, Huntsville, USA, 2003.

[14] Posner,F., "Distribution Functions for Temporal Measures of Sea Spike Characterization", *Proceedings International Conference on Radar 2004,* Toulouse, France, October 2004.

[15] Greco, M., Stinco, P., and Gini, F., "Identification and analysis of sea radar clutter spikes", *IET Radar, Sonar & Navigation,* 4, 2 (2010), 239-250.

[16] Rosenberg, L., "Sea-Spike Detection in High Grazing Angle X-Band Sea-Clutter", *IEEE Transactions on Geoscience and Remote Sensing,* 51, 8 (2013), 4556-4562.

[17] Arnold-Bos, A., Khenchaf, A., and Martin, A., "Bistatic Radar Imaging of the Marine Environment - Part I: Theoretical Background", *IEEE Transactions on Geoscience and Remote Sensing,* 45, 11 (2007), 3372-3383.

[18] Johnson, J.T., and Ouellette, J.D., "Polarization Features in Bistatic Scattering From Rough Surfaces", *IEEE Transactions on Geoscience and Remote Sensing,* 52, 3 (2014), 1616-1626.

[19] Palamà, R., Greco, M., Stinco, P., and Gini, F., "Statistical analysis of netrad high resolution sea clutter", *Proceedings of the 21st European Signal Processing Conference (EUSIPCO),* Marrakech, Morocco, 2013.

[20] Willis, N., and Griffiths, H.D., *Advances in bistatic radar*, SciTech Publishing, Raleigh, NC, 2007.

[21] Welch, P.D., "The use of fast Fourier transform for the estimation of power spectra: A method based on time averaging over short, modified periodograms", *IEEE Transactions on Audio and Electroacoustics*, 15, 2 (Jun. 1967), 70-73.

[22] Kay, S.M., *Fundamentals of Statistical Signal Processing, Estimation Theory, Vol. I*, Prentice Hall PTR, Upper Saddle River, New Jersey,1993.

[23] Stinco, P., Greco, M., and Gini, F., "Adaptive detection in compound-Gaussian clutter with inverse-gamma texture", *Proceedings of the IEEE CIE International Conference on Radar,* 434-437, Chengdu, China, 24-27 Oct. 2011.

List of Figures

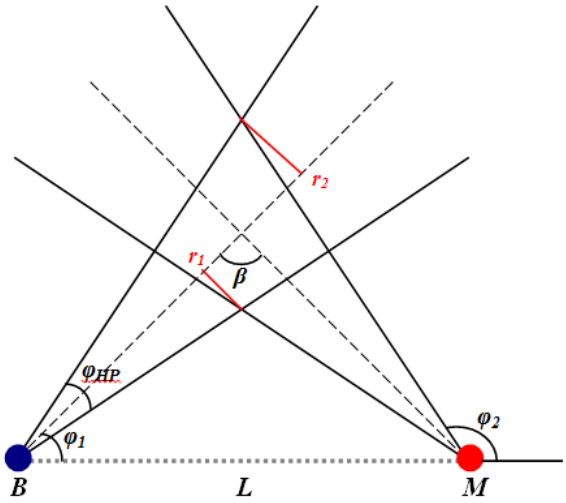

Fig.1 - Sketch of bistatic geometry (*B*: bistatic node, *M*: monostatic node, *L*: baseline, *β*: bistatic angle).

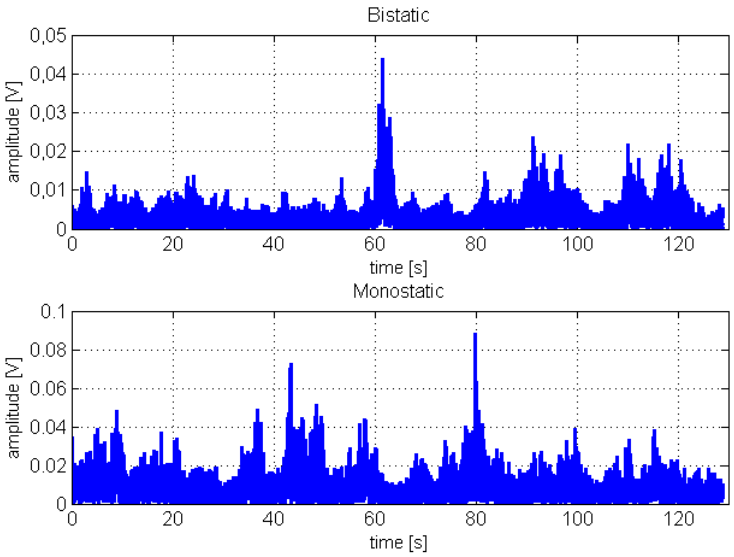

Fig.2 - Time History of the amplitude clutter samples. Dataset #4, VV polarization, $\varphi_1 = 60°$, r_{CUT} = 2000m.

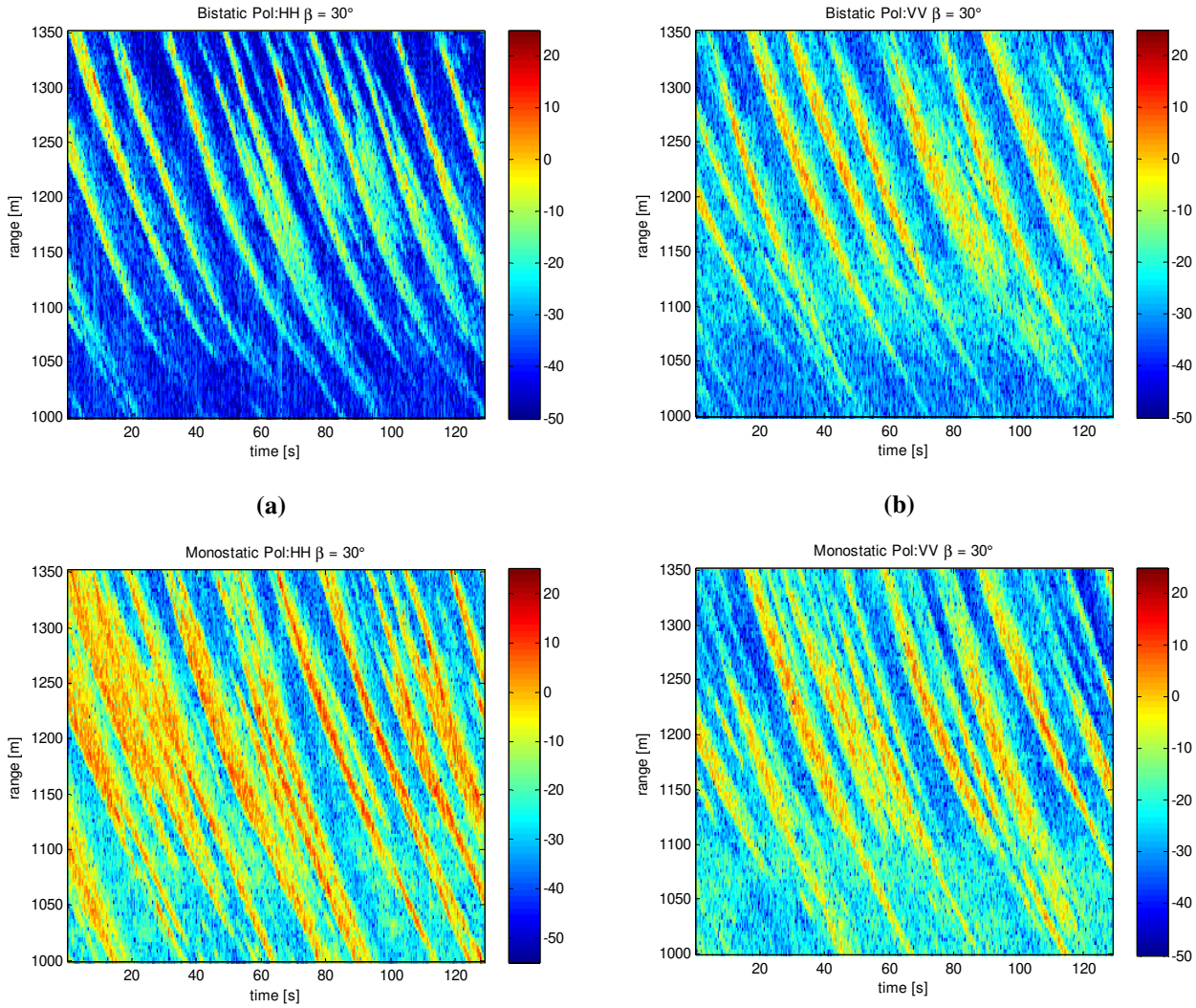

Fig.3 - Power-Range-Time maps β = 30°; (a) bistatic HH, (b) bistatic VV, (c) monostatic HH, (d) monostatic VV. Color scale: dBmW.

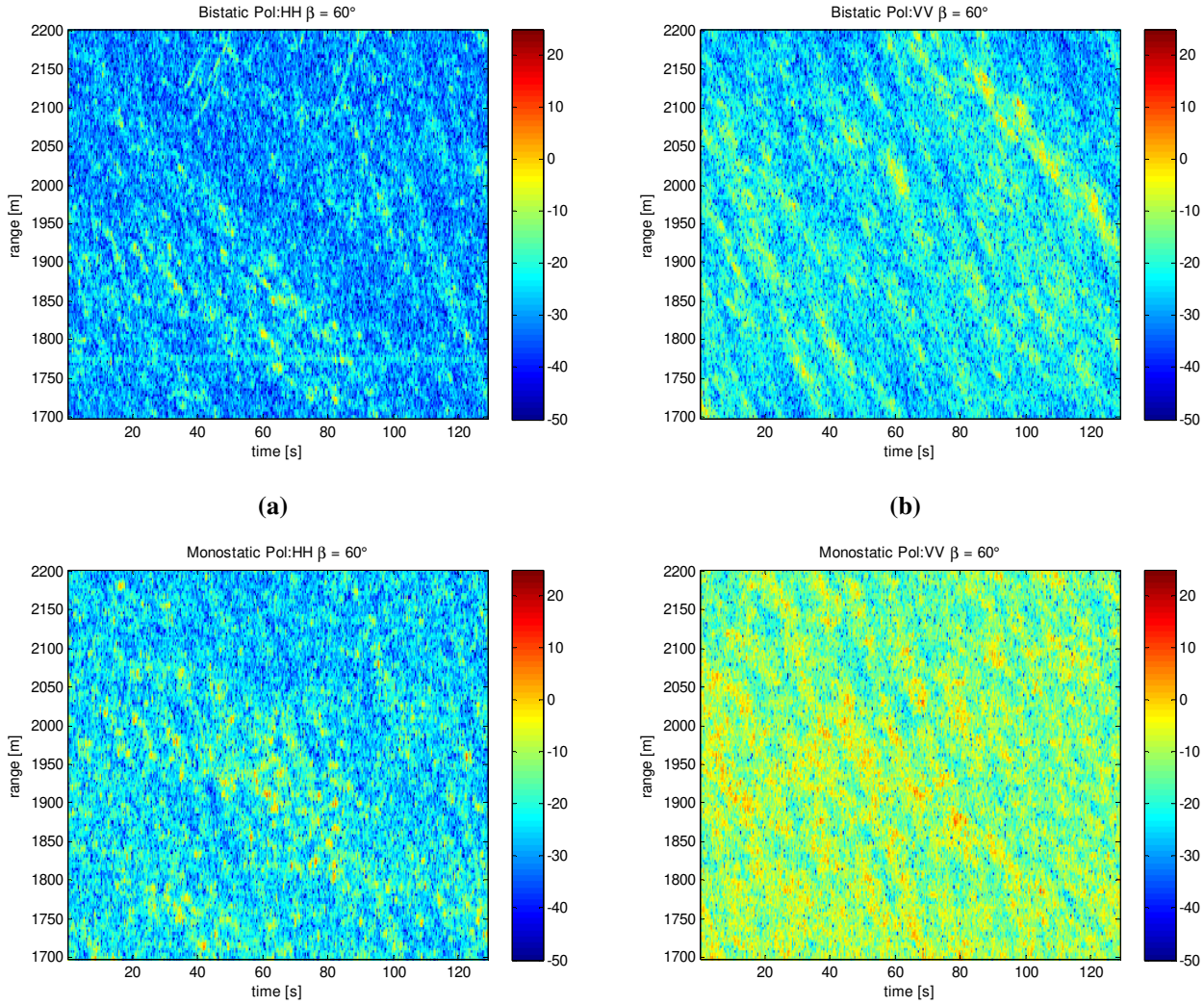

Fig.4 - Power-Range-Time maps $\beta = 60°$; (a) bistatic HH, (b) bistatic VV, (c) monostatic HH, (d) monostatic VV. Color scale: dBmW.

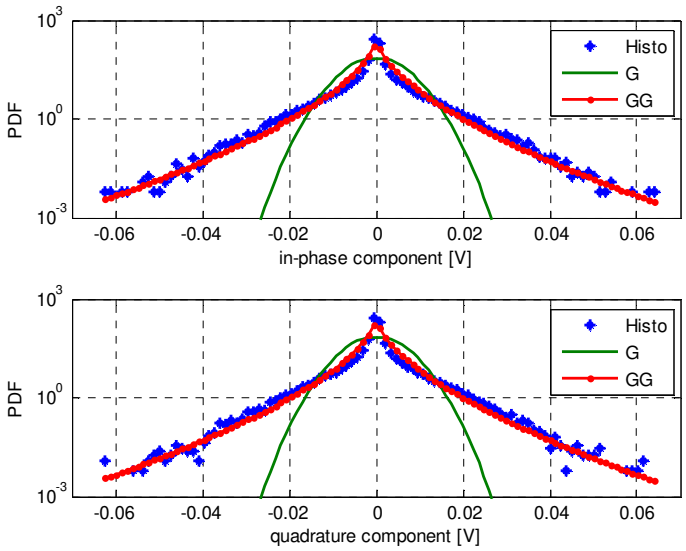

Fig.5 - Empirical Pdf of In-Phase (upper) and Quadrature (lower) clutter components. Dataset #5, bistatic HH data, azimuth pointing angle $\varphi_1 = 65°$, range cell r_{CUT} = 900m

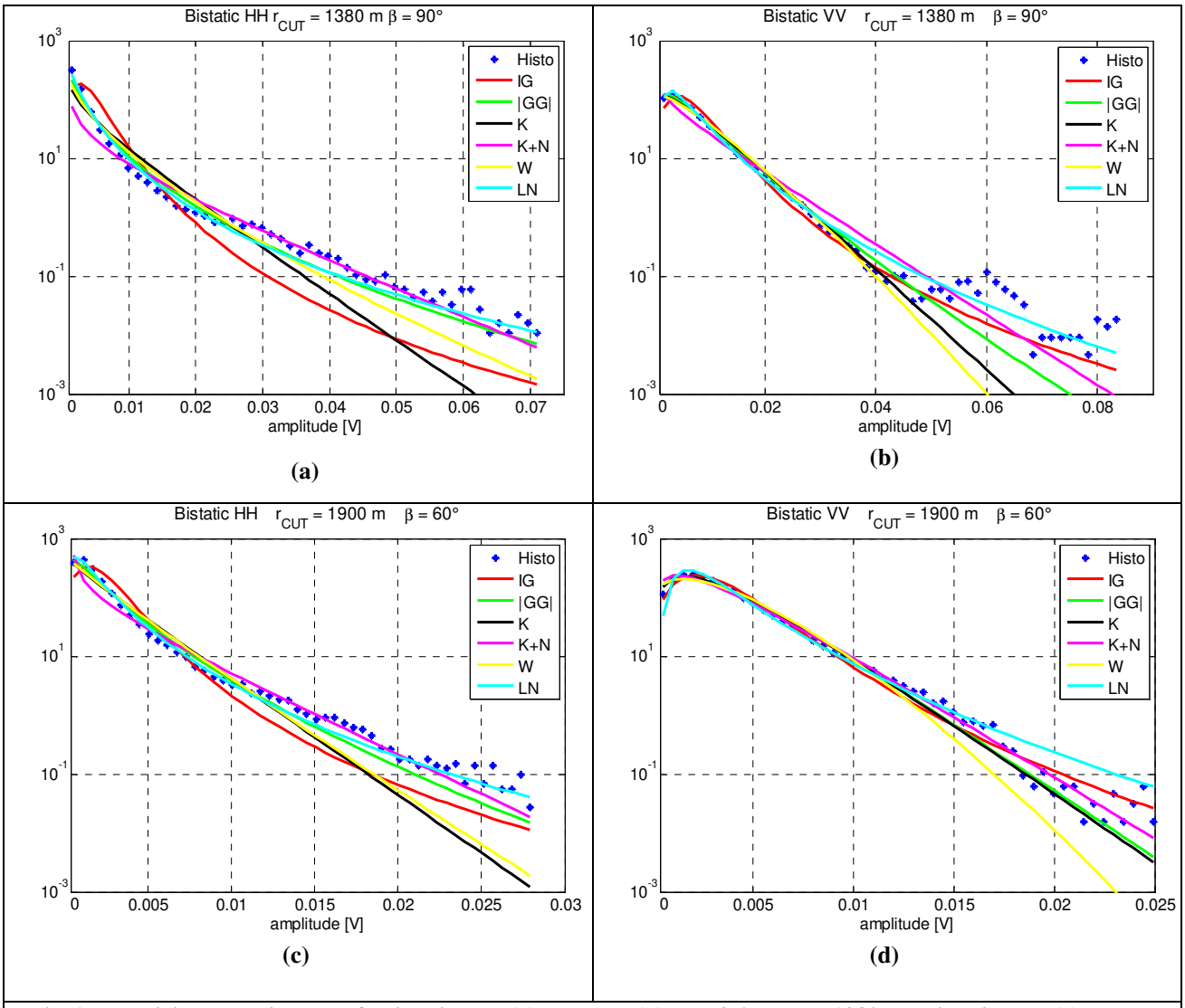

Fig.6 - Empirical amplitude pdf. Bistatic HH (a) and VV (b), φ_1=45°, r_{CUT} = 1380 m; bistatic HH (c) and VV (d), φ_1=60°, r_{CUT} = 1900 m.

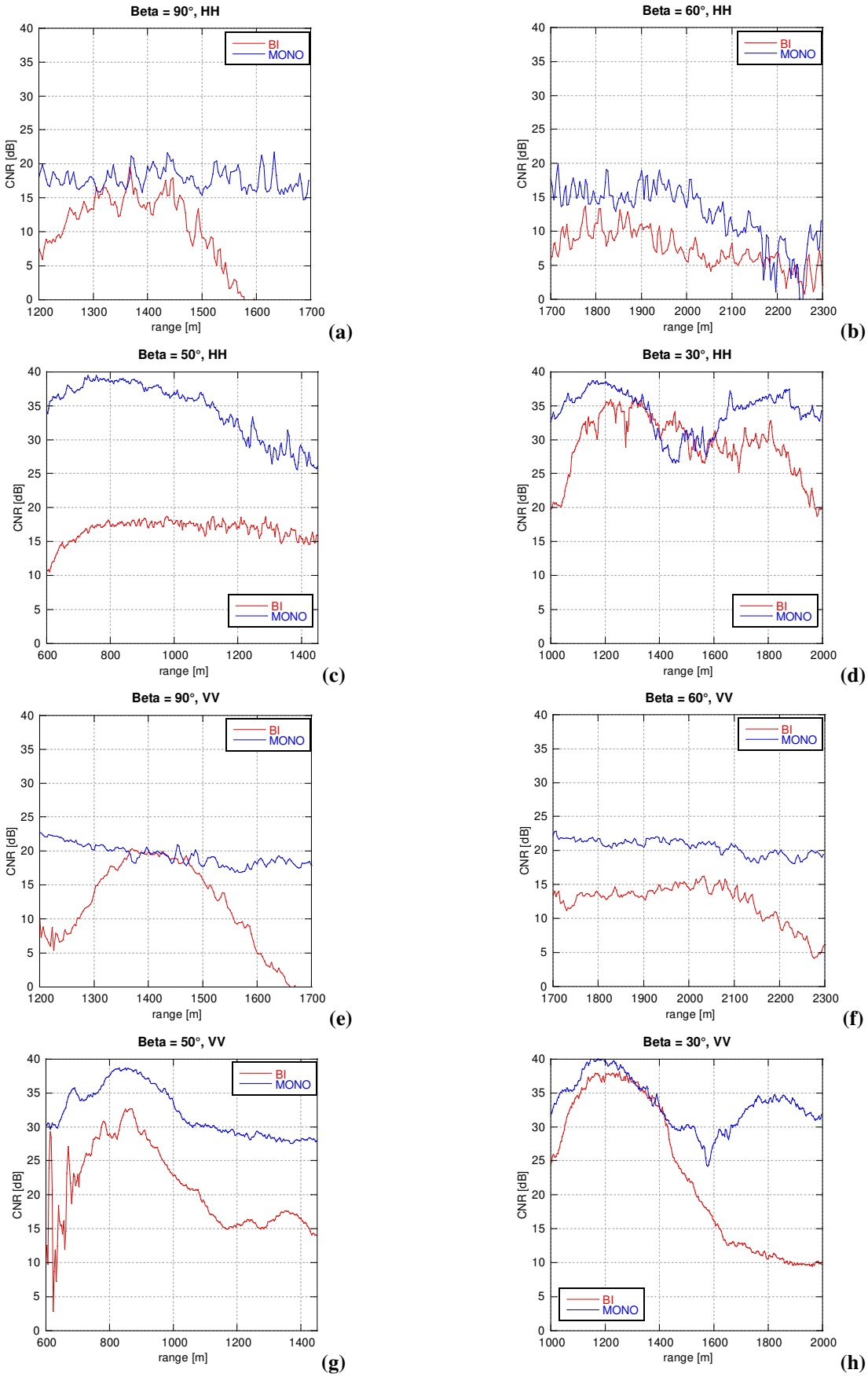

Fig.7 Clutter-to-Noise Ratio (CNR) vs range. (a) $\beta = 90°$ HH; (b) $\beta = 60°$ HH; (c) $\beta = 50°$ HH; (d) $\beta = 30°$ HH; (e) $\beta = 90°$ VV; (f) $\beta = 60°$ VV; (g) $\beta = 50°$ VV; (h) $\beta = 30°$ VV

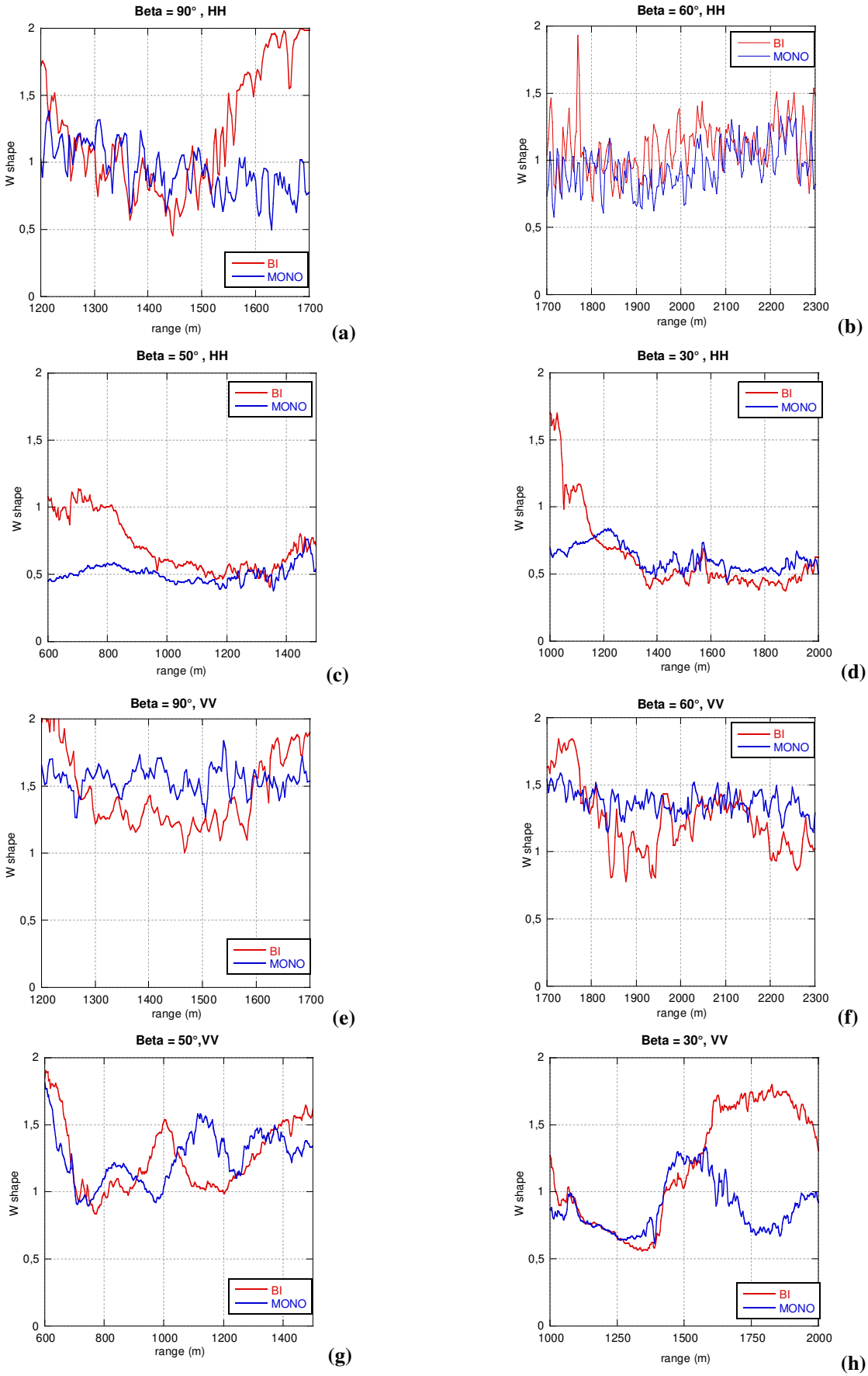

Fig.8 - Weibull Shape parameter vs range. (a) $\beta = 90°$ HH; (b) $\beta = 60°$ HH; (c) $\beta = 50°$ HH; (d) $\beta = 30°$ HH; (e) $\beta = 90°$ VV; (f) $\beta = 60°$ VV; (g) $\beta = 50°$ VV; (h) $\beta = 30°$ VV.

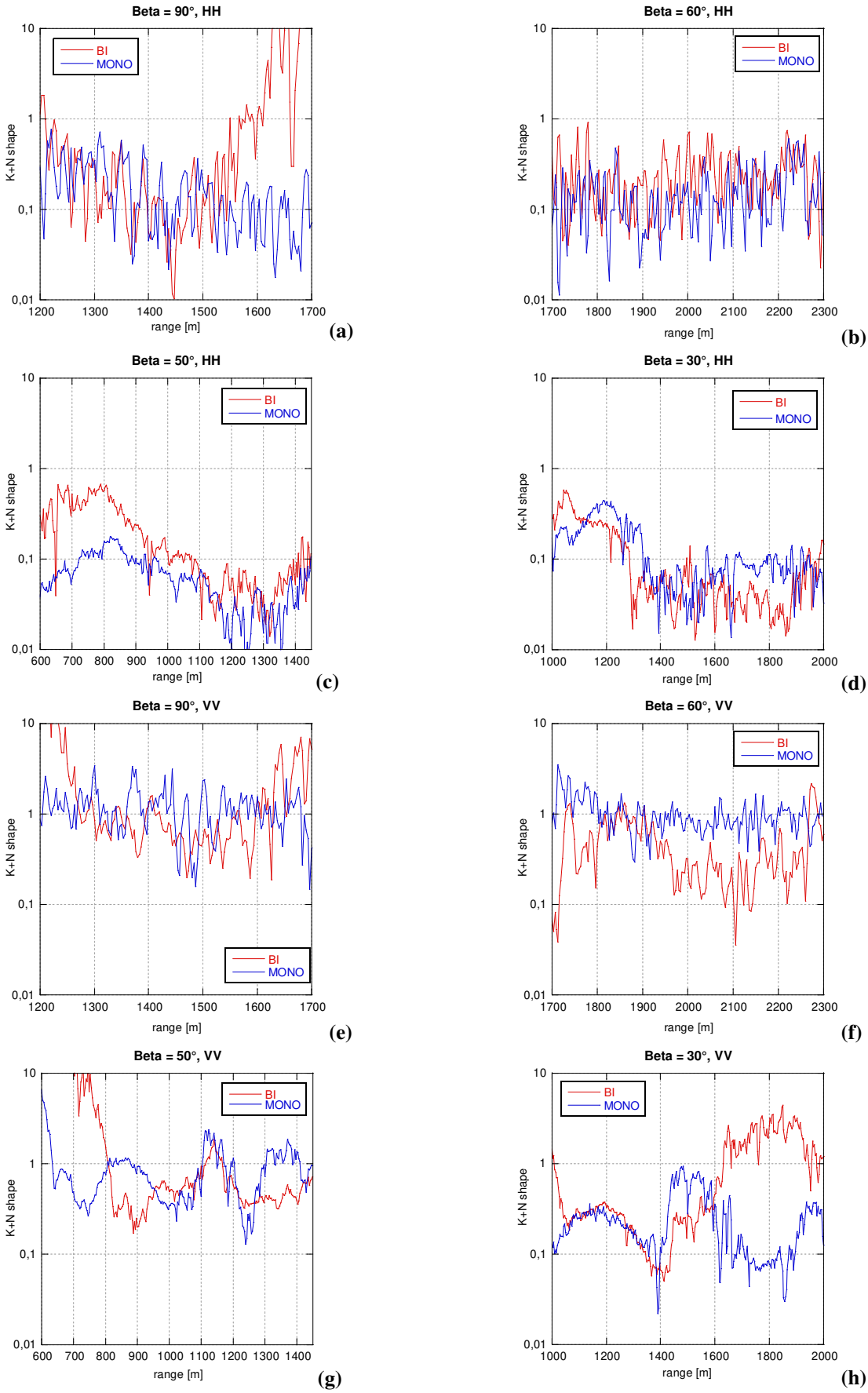

Fig.9 K-plus-Noise shape parameter vs range (a) $\beta = 90°$ HH; (b) $\beta = 60°$ HH; (c) $\beta = 50°$ HH; (d) $\beta = 30°$ HH; (e) $\beta = 90°$ VV; (f) $\beta = 60°$ VV; (g) $\beta = 50°$ VV; (h) $\beta = 30°$ VV.

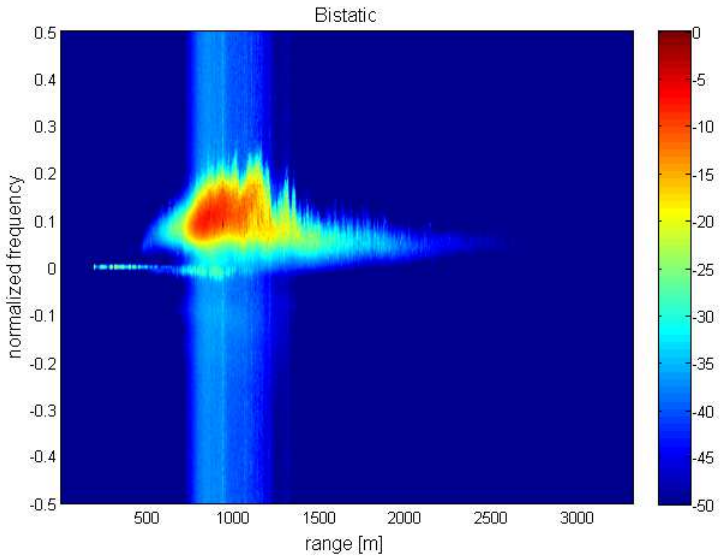

(a)

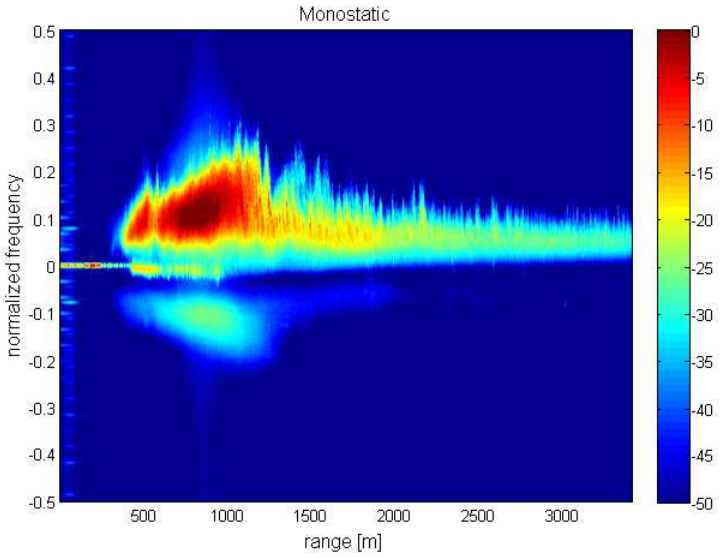

(b)

Fig.10 - Range-Doppler map of bistatic (a) and monostatic (b) data, HH polarization. bistatic angle β=50°.

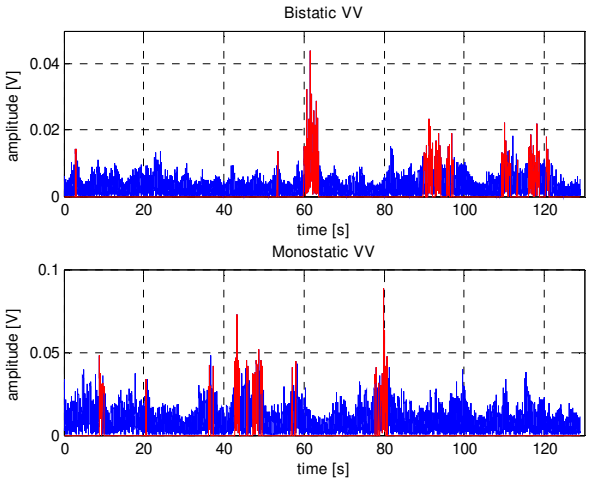

(a)

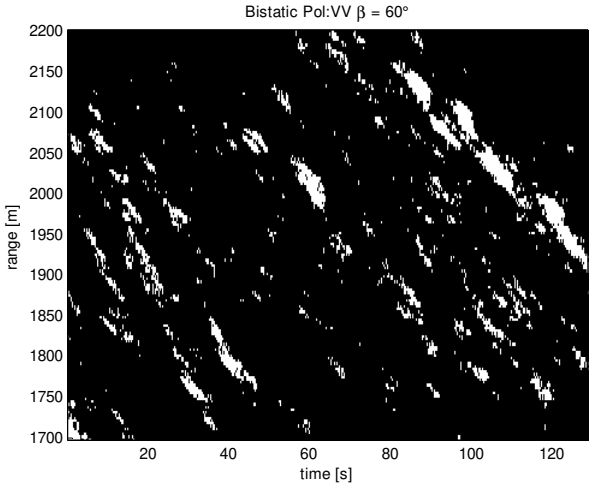

(b)

Fig.11 - (a) Time history of amplitude samples, with the selected spikes plotted in red (Dataset #4, VV data, range *r* = 2000 m, azimuth $\varphi_1 = 60°$); (b) mask of the selected spikes (Bistatic VV, $\beta = 60°$).

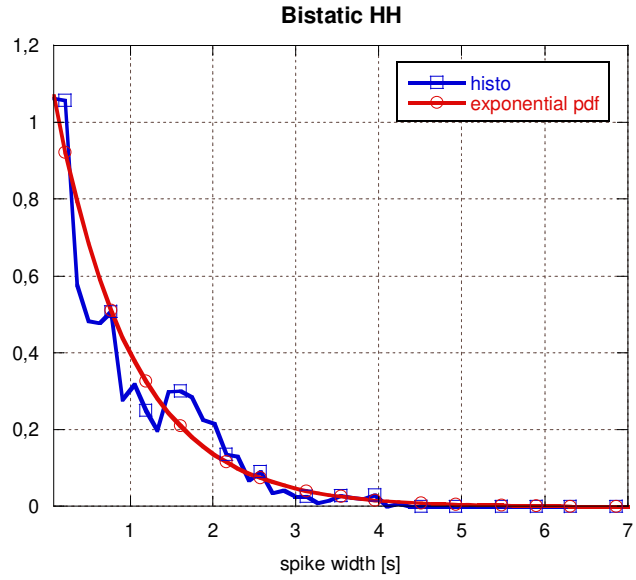

Fig.12 - Empirical pdf of spike width (bistatic HH data, β=30°).

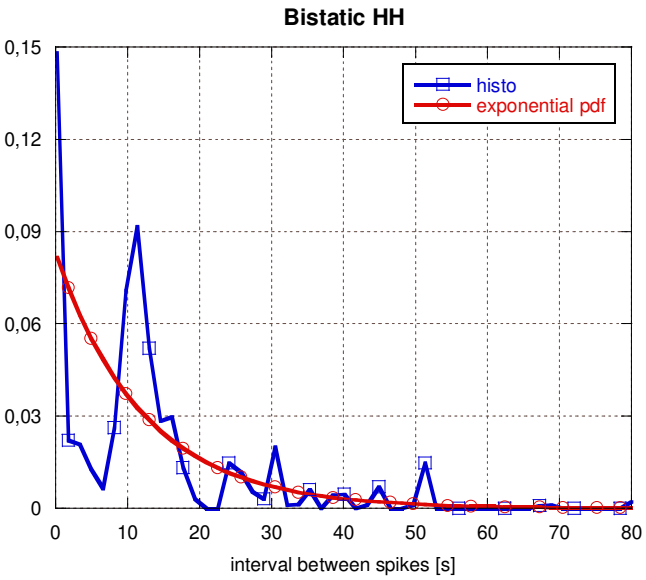

Fig.13 - Empirical pdf of interval between spikes (bistatic HH data, β=30°).

List of Tables

Radar Parameters	
Carrier Frequency	2.4 GHz
Transmitted Signal	Up/Down Chirp
Bandwidth	45 MHz
Pulse Duration	Variable
Pulse Repetition Frequency	1 KHz
Range Resolution	3.33m
Sampling Frequency	100 MHz
Polarization	HH,VV (separately)
Half Power Beamwidth	9° (el.) x 11° (az.)

Tab.1 - NetRad Parameters.

# Dataset	Day (dd/mm/yy)	Time (hh/mm/ss)	φ_1	φ_2	Pol	L (m)	β
1	10/10/10	12/44/20	45°	135°	HH	1827	90°
2	10/10/10	16/03/00	45°	135°	VV	1827	90°
3	10/10/10	12/33/00	60°	120°	HH	1827	60°
4	10/10/10	15/51/50	60°	120°	VV	1827	60°
5	21/10/10	17/30/00	65°	115°	HH	728	50°
6	21/10/10	19/55/00	65°	115°	VV	728	50°
7	21/10/10	19/01/00	75°	105°	HH	728	30°
8	21/10/10	19/27/55	75°	105°	VV	728	30°

Tab.2 - Summary of the analyzed datasets.

	Bi HH		Mono HH		Bi VV		Mono VV	
	I	Q	I	Q	I	Q	I	Q
β=90° r_{CUT}=1400m	30.57	31.11	41.53	42.69	6.27	6.36	5.89	6.01
β=60° r_{CUT} =1900m	31.67	30.52	25.23	20.70	9.71	9.73	5.66	6.00
β=50° r_{CUT} = 900m	16.33	16.34	34.88	34.99	16.52	16.54	6.47	6.47
β=50° r_{CUT} = 1400m	55.29	55.48	63.59	62.94	51.39	51.29	54.09	54.02

Tab.3 - Values of kurtosis averaged over an interval of ten range cells, centered on r_{CUT}.

	Bi HH	Mono HH	Bi VV	Mono VV
β=90° r_{CUT} = 1400m	0.141	0.172	0.981	1.181
β=60° r_{CUT} = 1900m	0.161	0.079	0.756	0.801
β=50° r_{CUT} = 900m	0.226	0.094	0.229	0.872
β=30° r_{CUT} = 1400m	0.047	0.057	0.064	0.091

Tab.4 - Values of the K+N shape parameter averaged over an interval of ten range cells, centered on r_{CUT}

	Bi HH	Mono HH	Bi VV	Mono VV
β=90°	5%	5.3%	7.1%	3.4%
β=60°	6.1%	5.3%	6.6%	5.1%
β=50°	11.8%	9.9%	6.4%	14.3%
β=30°	8.4%	13.3%	11.9%	12.2%

Tab.5 - Percentage of the number of spikes with respect to the number of total samples.

	Bi HH/Mono HH	Bi VV/Mono VV	Bi HH/Bi VV	Mono HH/Mono VV
β=90°	0.95	2.11	0.71	1.57
β=60°	1.14	1.31	0.92	1.06
β=50°	1.19	0.45	1.86	0.70
β=30°	0.63	0.98	0.71	1.09

Tab.6 Relative number of spikes

	Bi HH	Mono HH	Bi VV	Mono VV
β=90°	0.459	0.371	0.442	0.318
β=60°	0.439	0.406	0.556	0.368
β=50°	0.959	1.220	0.816	0.578
β=30°	0.935	0.750	1.215	1.001

Tab.7 - Mean spike width [s].

	Bi HH	Mono HH	Bi VV	Mono VV
β=90°	8.284	6.092	6.068	9.394
β=60°	7.497	7.368	6.959	6.517
β=50°	7.965	11.867	8.934	5.776
β=30°	12.222	6.514	14.128	8.561

Tab.8 - Mean interval between spikes [s].